PAPER

Check for updates

Understanding the electrochemical behaviour of reduced graphene oxide cathodes in all-carbon Na-ion batteries†

Marcin W. Orzech, [ID] [a] Francesco Mazzali,[a] Arturas Adomkevicius,[a] Mauro Coduri, [ID] [b] Yubiao Niu,[c] James D. McGettrick, [ID] [c] Philip A. Chater, [ID] [d] Laura Cabo-Fernandez,[e] Laurence J. Hardwick,[e] Lorenzo Malavasi [ID] [b] and Serena Margadonna [ID] *[a]

Sodium-ion batteries represent a sustainable and cost-effective solution for grid-scale energy storage. However, the reliance on cathode materials containing scarce transition metals currently limits their wider adoption. Carbonaceous materials present an environmentally sustainable and economically viable alternative. This study investigates the application of reduced graphene oxide as a cathode active material. A detailed analysis of the storage mechanism and its dependence on the morphological and chemical structure revealed that it combines surface capacitance and faradaic reactions. The key factors responsible for high capacity and long cycle life are the open structure of graphene sheets and the presence of functional oxygen and nitrogen groups where Na+ ions are stored in the $R-C=O + Na^+ + e^- \leftrightarrow R-C-O-Na$ reaction. A good understanding of the mechanism allowed optimisation of cycling conditions in a proof-of-concept all-carbon full cell incorporating reduced graphene oxide and hard carbon as a cathode and an anode, respectively. The system displays good energy density (80 W h kg^{-1}) and remarkable stability over 500 cycles. The gained insights will support the rational design of more efficient carbonaceous electrodes.

Introduction

Lithium-ion batteries (LIBs) are dominating the portable electronics and electric vehicles (EVs) markets. However, the booming development of the latter has raised concerns about the increasing demand for precursor materials. A dominant fraction of LIB production costs (~36% of total cost) is contributed by the high-performance cathodes, particularly those containing Co, Mn and Ni.[1] Matching the supply of these metals with the rapidly increasing demand is challenging and raises questions on the sustainability of the technology. These issues inspired research on so-called 'beyond Lithium' batteries based on elements that are more abundant. Among these, the most

promising are sodium-ion batteries (SIBs), which are currently heavily investigated as a viable and sustainable alternative to LIBs, particularly for medium- to large-scale energy storage applications.[2–5]

The most studied electrode materials for SIBs are hard carbons as anode active materials and a few groups of cathodes: transition metal oxides, polyanions, and Prussian Blue analogues. Hard carbons are an effective and sustainable substitution for expensive graphite used in LIBs.[6–9] On the other hand, the cathodes often contain transition metals (including cobalt) presenting the same concerns and limitations in terms of cost and sustainability as those currently employed for LIBs. Furthermore, most of the intercalation compound cathodes, also considering phosphates and fluorides, suffer from either low sodium storage capacity and rate capability or poor cycle life.[10,11]

A promising solution to sustainability and cost concerns as well as performance limitations is the use of carbon as the active material for both electrodes.[12] Carbonaceous materials are inexpensive, environmentally friendly and highly conductive. Recent works on the utilization of organic or carbonaceous materials as cathodes for LIBs, such as aromatic carbonyl derivative polymers,[13] functionalised carbon nanotubes (CNTs)[14,15] and reduced graphene oxide (rGO)[16–20] showed promise for 'green' and sustainable batteries. Nevertheless, research on applying this

[a] *Future Manufacturing Research Institute, College of Engineering, Swansea University, Swansea, SA1 8EN, UK. E-mail: S.Margadonna@swansea.ac.uk*

[b] *Department of Chemistry and INSTM, University of Pavia, 27100 Pavia, Italy*

[c] *AIM and SPECIFIC, College of Engineering, Swansea University, Swansea, SA1 8EN, UK*

[d] *Diamond Light Source Ltd, Diamond House, Harwell Science and Innovation Campus, OX11 DE Didcot, UK*

[e] *Stephenson Institute for Renewable Energy, Department of Chemistry, University of Liverpool, L69 7ZD, Liverpool, UK*

† Electronic supplementary information (ESI) available. See DOI: https://doi.org/10.1039/d4ma00605d

approach in Na-ion batteries is still lagging behind and focuses mostly on the negative electrode side.[21]

Recently, Ali *et al.* reported on the electrochemical performance of rGO as a suitable cathode for SIBs.[22] It showed a high specific capacity of 235 mA h g^{-1} and stable behaviour over 1000 cycles. The authors ascribed the outstanding performance to pseudocapacitive storage and reversible sodium adsorption on graphene layers, which benefits from the high surface area of the material. Notably, it was the first time that rGO was used as the only active material for the Na-ion cathode, instead of as an additive that enhances the performance of the electrode.[21,23–25] Another work on hollow graphene nanospheres demonstrated that the surface mechanism of Na$^+$ ion reactions with functional groups improved the specific capacity of the cathode and allowed stable cycling at very high current rates of up to 40 A g^{-1}.[26] The reported mechanism is similar to reversible redox reactions with oxygenic functional groups observed in functionalised carbon electrodes for LIBs.[27–31] The most commonly reported energy storage mechanisms observed in carbonaceous cathodes are either intercalation in dual-ion type cells[32–35] or electrical double-layer capacitive (EDLC) storage in supercapacitors.[36] However, reports on rGO more often point to a combination of pseudocapacitive behaviour and surface redox reactions with functional groups.[37–39] The fundamental understanding of these mechanisms is still lacking, which hinders the rational design of carbonaceous cathode materials.

This work investigates the underlying mechanism in detail and applies the gained knowledge to construct an all-carbon full cell with excellent stability. Two reduced graphene oxide cathodes, differing in morphology and chemical structure, were investigated for their potential use in SIBs. The primary energy storage mechanism in both cases was found to be absorption. However, by the use of *in situ* Raman spectroscopy and X-ray pair distribution function (PDF), additional processes were identified that contribute to good performance. They involved surface faradaic reactions between the sodium ions and the functional groups as well as the bipolar behaviour of rGO resulting in additional capacitive storage of ClO$_4^-$ anions. This discovered hybrid energy storage mechanism results in a significantly increased gravimetric capacity. A proof-of-concept all-carbon full cell with rGO as the cathode and hard carbon (HC) as the anode, showed a specific energy of 80 W h kg^{-1} and high stability over 500 cycles, confirming that rGO is a viable cathode material for SIBs. These findings support the way to the design and development of more sustainable energy storage systems.

Experimental

Material synthesis and characterization

The reduced graphene oxide powders were acquired from two different companies: Graphenea Inc. (rGO_1) and Ossila Ltd. (rGO_2). The received powders were dispersed in water at a concentration of 0.5 g dm^{-3} and sonicated for 6 h. Consequently, they were dried and used as active material in electrodes. The X-ray powder diffraction (XRD) patterns of materials

and electrodes were measured using a Bruker D8 Advance diffractometer with a Cu Kα radiation source (λ = 1.5406 Å). The Brunauer–Emmett–Teller (BET) method was used to measure the specific surface area of the rGO powders by N$_2$ adsorption (77.3 K) using Micromeritics TriStar II (TriStar II 3020 V1.04). The surface analyses were performed by means of X-ray photoelectron spectroscopy (XPS, Kratos Axis Supra) using focused monochromatic 225W Al Kα radiation ($h\nu$ = 1486.6 eV). The high-resolution peaks were recorded with a constant pass energy of 40 eV. The analysis area was limited by an aperture to a 110 μm diameter circle. Photoelectron spectra were recorded using Casa XPS software with Shirley backgrounds and 30% Gaussian and 70% Lorentzian curves. The binding energy (BE) scale was calibrated from the adventitious carbon using the C 1s peak at 284.8 eV. Quantification was performed using the Kratos relative sensitivity factor (R.S.F.) library. Raman spectra were recorded using a Raman microscope (Renishaw inVia), using a 532 nm wavelength laser focused using an inverted microscope (Leica), *via* a 50× objective lens (Leica). Scanning electron microscopy (SEM) imaging was performed using a ZEISS Evo scanning electron microscope. The accelerating voltage was 15 kV and the working distance was ∼10 mm. Scanning transmission electron microscope (STEM) images and energy-dispersive X-ray spectroscopy (EDX) line scans were obtained using an FEI Talos (F200X) microscope, operating in high-angle annular dark-field (HAADF) mode at 200 kV.

Electrochemical characterization

The electrodes consisted of active material, carbon black (Super P, Imerys) and PVDF binder in a ratio of 8 : 1 : 1, respectively. The cycling was performed in half-cells with sodium metal anode and 1 M solution of NaClO$_4$ (98%, Sigma) in ethylene carbonate (anhydrous, 99%, Sigma) and propylene carbonate (anhydrous, 99.7%, Sigma) in a 1 : 1 volume ratio as electrolyte. Electrochemical performances were evaluated using standard CR2032 coin cells. Galvanostatic cycling was performed in a potential range of 1.2 V to 4.5 V *vs.* Na/Na$^+$ (as in previous work on the rGO cathode[22]) using a Maccor cycler. For the *ex situ* XRD measurements, the cells were disassembled after one cycle in an Ar filled glovebox, and the electrodes were washed with EC:PC and sealed in a glass capillary. For the full cell assembly, hard carbon was used as the anode. Hard carbon was synthesized with the addition of GO as a dehydration agent. In particular, 6.4 g of sucrose was added to 100 mL of graphene oxide stock 0.8 g L^{-1} (Graphenea) and sonicated for 3 hours. Subsequently, the solution was dried and the resulting powder was dehydrated at 180 °C for 24 hours. Following pyrolysis in Ar at 1100 °C the obtained hard carbon was collected. The anode slurry had the same PVDF and carbon black ratio as the cathode. Between the cathode mass and the anode mass, a ratio of 0.9 was maintained. The rGO_2/CMC cathode was presodiated for 30 minutes in a short circuit with a sodium metal disc in 1 M NaClO$_4$ in the EC:PC electrolyte. Galvanostatic cycling was performed between 0.5–3.7 V at 30 mA g^{-1} based on the active mass of the rGO in the cathode. A schematic

representation of the process for full cell (rGO_2/HC) assembly is provided in the ESI† (Fig. S1).

In situ measurements

For the *in situ* Raman spectra measurements, free standing electrodes were prepared. The active material, PVDF and dibutyl phthalate (DBP) in 40 : 30 : 30 ratio, respectively, were dispersed in acetone and cast onto glass at a wet thickness of 600 μm. After drying, DBP was removed with diethyl ether, leaving porous electrodes. No carbon black additive was used to avoid its influence on the collected spectra. The electrodes were transferred to an Ar filled glovebox and assembled in an EL-CELL spectroelectrochemical Raman cell (ECC-Opto-Std) with Na metal as counter and reference electrodes.[40,41] The cell enables *in situ* investigation of electrochemical processes in an inert atmosphere. The Raman laser was focused upon the electrode's back surface during cyclic voltammetry, and spectra were obtained as a function of potential. The acquisition area was selected in a manner to ensure minimal detection of Raman peaks from the electrolyte. Cyclic voltammetry was performed in 1.2–4.5 V potential range at a scan rate of 0.2 mV s^{-1} using the Bio-Logic VMP3 potentiostat.

For the *in situ* X-ray pair distribution function (PDF) measurements, the same free standing electrodes were used. The in-house made Swagelok-type cells provided by beamline were assembled with Na metal counter electrode and a glass-fibre separator (Whatman, GF/D). In the used radial geometry, it is possible to slice just through the electrode of choice and get data from electrodes as thin as 50 microns. The cells were cycled galvanostatically at a rate of C/10 in the range of 1.0 to 4.5 V. X-ray total scattering data were collected with an exposure time of 120 s. Data were collected for the first sodiation, the first desodiation, and the second sodiation. X-ray scattering data were collected at the I15-1 beamline at the diamond light source using an X-ray energy of 76.7 keV ($\lambda = 0.1617$ Å) and a flat panel detector (CeO$_2$ standard). The experimental 2D raw images were automatically reduced at the beamline. All scattering contributions but the signal coming from the rGO cathode, such as empty cell, electrolyte and separator were subtracted. PDFs were computed using the PDFgetX3 software.[42] Data were truncated to $Q_{max} = 24$ Å^{-1} before Fourier Transform.

## Results and discussion

Materials characterization

The two reduced graphene oxide (rGO) powders investigated were obtained by chemical reduction and are commercially available. The choice of using these materials, instead of producing in-house optimized rGO, was driven by the idea of mimicking scale-up conditions for electrode manufacturing that requires the market availability of large amounts of active materials. The morphology and structure of the two samples, herein identified as rGO_1 and rGO_2, were structurally characterized using powder X-ray diffraction (XRD), Raman spectroscopy, X-ray photoelectron spectroscopy (XPS) and electron microscopy. The diffraction

profiles of both samples (Fig. 1(A)) show the characteristic broad peak of rGO at $2\theta \sim 25.0^\circ$, which is related to the graphitic [002] plane. From its position and width, it is possible to estimate the values of the interplanar distance (d_{002}) and the crystallite height (L_c) corresponding to the average height of the stacking layers.[19] For rGO_1, the values of $d_{002} = 0.36$ nm and $L_c = 0.91$ nm, corresponding to ~ 2–3 graphene layers,[43] were calculated. An average diameter of the stacking layers $L_a = 6.2$ nm was also obtained by fitting the peak at $2\theta \sim 43.0^\circ$, which is related to the two-dimensional (10) reflection, giving an indication of short-range order within the stacked graphene layers. The diffraction profile of rGO_2 shows broader peaks suggesting a higher degree of disorder both within the layers and along the stacking direction. The interplanar distance $d_{002} = 0.35$ nm and the average height of 0.62 nm (~ 1–2 graphene layers) were obtained.

Investigations of the chemical composition and structure of the two samples were performed through X-ray photoemission spectroscopy (XPS). The high resolution C1s, N1s and O1s (Fig. 1(D)–(I)) spectra were recorded to highlight the presence of different oxygen and nitrogen containing functional groups. The C1s spectra show a very similar distribution between sp^2 (C=C) and sp^3 (C–C) hybridization. On the other hand, the oxygen and nitrogen contents vary between samples, reflecting a difference in the functional groups. The O/C ratios are 0.15 and 0.13 for rGO_1 and rGO_2, respectively, which shows that after reduction more oxygenic functional groups remained in the former. However, to get a better idea on the total content of functional groups also nitrogen should be considered. The O + N/C ratios are 0.16 and 0.17 for rGO_1 and rGO_2, respectively, which reveals that the latter is slightly more functionalised. Comparing the fitted envelopes, it can be inferred that rGO_2 contains less epoxide (C–O–C) and carboxyl (HO–C=O) groups, but a higher amount of carbonyl (C=O) functional groups than rGO_1. The amount of hydroxyl (C–OH) groups is comparable in both materials. The two samples present a clear difference in nitrogen content −0.6% and 3.3% for rGO_1 and rGO_2, respectively. The only nitrogen bonds detected in the former were pyrrolic N, while in rGO_2, all three – pyridinic, pyrrolic and graphitic–nitrogen bonds were present, with pyrrolic N (1.5%) and pyridinic N (1.2%) dominating. It has been reported that the introduction of N atoms, particularly pyrrolic and pyridinic, causes more edges as well as open and flexible vacancy defects for increased reversible Li$^+$ and Na$^+$ ions storage in graphene cathodes.[37,44,45]

Raman spectroscopy is one of the most insightful techniques for characterisation of carbonaceous materials. The Raman spectra of both samples were recorded at an excitation wavelength of 532 nm (Fig. 1(B) and (C)). They demonstrate the typical fingerprint of D (~ 1350 cm^{-1}) and G (~ 1590 cm^{-1}) bands found in sp^2 carbons. Spectra were fitted with 5 peaks, in analogy with previous work.[46,47] Besides D and G, the other three peaks are D′, A and D* (Table S2, ESI†). The D′ feature is another E$_{2g}$ graphitic lattice mode and has been attributed to disorder in a surface layer, *i.e.* graphene layers which are not directly sandwiched between two other graphene layers.[48,49] The $I_{D'}/I_G$ ratio has been assigned to the intercalation between carbon

Paper

Materials Advances
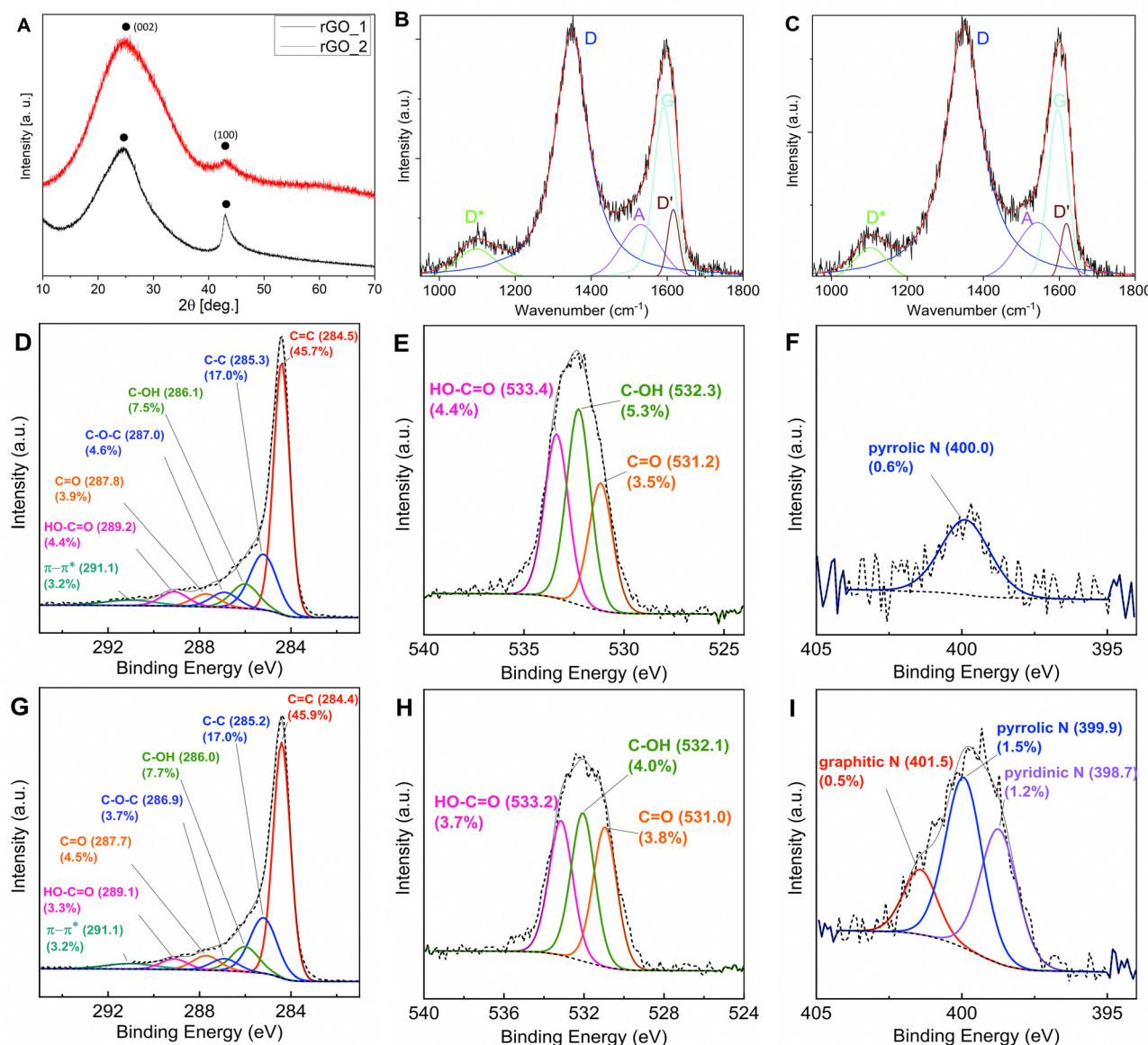
Fig. 1 Characterization of two different rGO materials, (A) X-ray diffraction pattern of rGO_1 and rGO_2 (black dots indicate peaks of rGO). (B) and (C) Raman spectrum of rGO_1 (B) and rGO_2 (C) in G and D bands region with 5 fitted peaks. (D)–(F) XPS spectra of rGO_1 in the C 1s region (D), O 1s region (E) and N 1s region (F). (G)–(I) XPS spectra of rGO_2 in the C 1s region (G), O 1s region (H) and N 1s region (I).

layers[50] or covalent bonding on the surface of the CNTs.[51] The A band is located around 1500 cm^{-1} and corresponds to amorphous carbon;[46,47,49] furthermore Claramunt et al. correlated the inversely proportional relation of I_A/I_G and FWHM of the A band to the crystallinity of rGO.[47] The D* band is located between 1100 and 1200 cm^{-1} and is related to an additional defect mode provided by sp^2–sp^3 bonds at the edges of networks.[52] Particularly, the I_{D^*}/I_G ratio increase corresponds to an increase in the number of sp^3 bonds at the edges of graphene sheets.[47]

The data derived from fitting the Raman spectra of the raw powders are summarised in Table S2 (see the ESI†). The relative intensity ratio of the main peaks (I_D/I_G) can be used to estimate the defect concentration.[53,54] Slightly higher value of the I_D/I_G ratio in rGO_2 (1.50) compared to rGO_1 (1.45), and broader D band suggests more a disordered nature of the rGO_2 sample,

which is in agreement with the XRD and the higher O + N/C ratio derived from XPS measurements. The defects on the graphitic surface layers are indicated by the $I_{D'}/I_G$ ratio, which is higher for rGO_1 (0.40) compared to 0.33 for rGO_2 (0.33). The XPS results suggest that this difference comes from more epoxy functional groups in rGO_1, which develop at the basal plane of the graphene sheets creating the in-plane defects and disorder.[55,56] Very close values of I_A/I_G and I_{D^*}/I_G reveal similar crystallinity and concentration of edge bonds in both samples.

The morphologies of the two materials were studied using electron microscopy (Fig. 2). From the SEM images, it can be clearly seen that rGO_2 (Fig. 2(D)) adopts the form of large flakes sized 0.1–1 μm comprising ultra-thin graphene oxide sheets (<1 nm). Large channels and voids formed by the sheets are clearly visible and creating an interconnected 3D porous
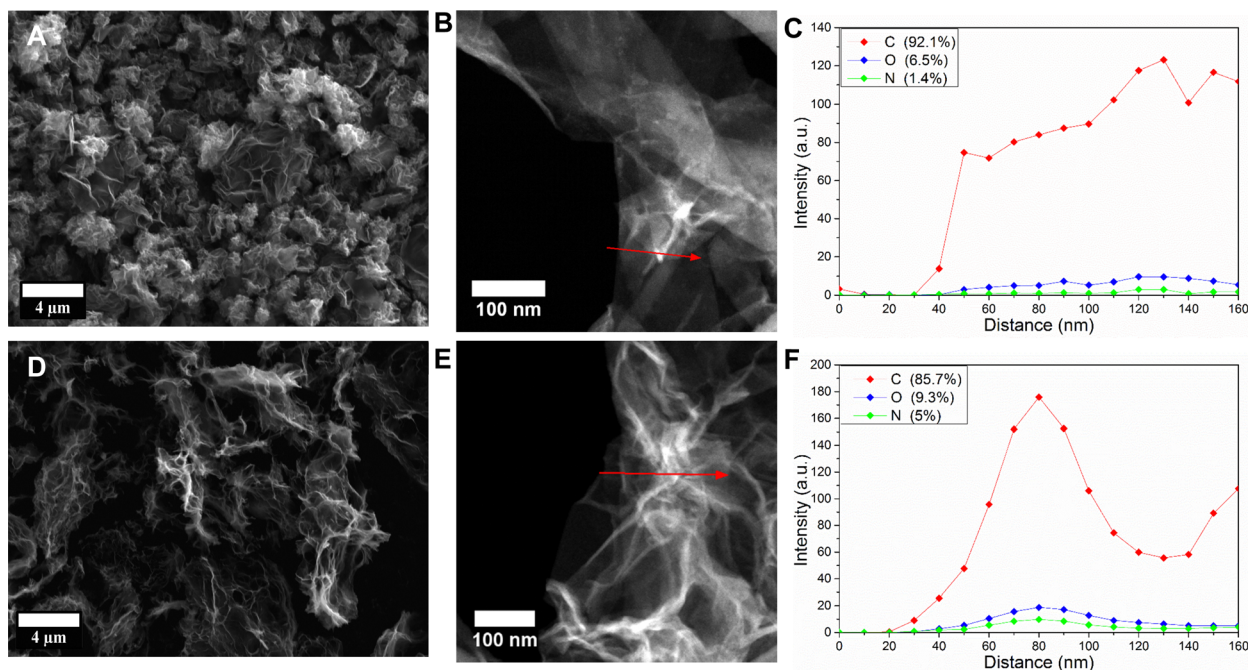
Fig. 2 Electron microscopy characterization of two different rGO materials. (A), (B), (D), (E) SEM and high-angle annular dark-field STEM images of rGO_1 (A), (B) and rGO_2 (D), (E) samples. (C), (F) The corresponding TEM EDX line scans of rGO_1 (C) and rGO_2 (F). Red arrow indicates the path of line scan.

network. Instead, rGO_1 (Fig. 2(A)) presents a bulkier morphology with particles that are a few micrometres in size. Thin graphene layers are clearly observed; however, they are agglomerated into closed structures. These morphological differences are significant, as rGO_2's large, thin flakes and porous network contrast sharply with rGO_1's bulkier and more agglomerated structure. This distinction is crucial for applications requiring high surface area and efficient electrolyte penetration. The more open and dispersed structure is additionally confirmed by the higher specific surface area (BET) of rGO_2 (865 ± 29 m^2 g^{-1}) than rGO_1 (461 ± 38 m^2 g^{-1}). For comparison, the reduced graphene oxide studied by Ali et al.[22] had a specific surface area of 789 m^2 g^{-1}. The high specific surface area and porous interconnected network are generally considered beneficial for short ion diffusion paths. Fig. 2(C) and (F) show the high-angle annular dark-field (HAADF) scanning transmission electron microscope (STEM) images and the corresponding energy-dispersive X-ray spectroscopy (EDX) line scans of rGO_1 and rGO_2, respectively. The rGO_2 flake in Fig. 2(E) is extensively creased, which creates many inner voids, while the rGO_1 flake presented in Fig. 2(B) has a smoother morphology. The EDX line profiles confirmed the presence of functional groups in both samples. The total content of oxygen and nitrogen was higher in rGO_2 (14.3%) than in rGO_1 (7.9%). Although the EDX measurements of such light elements have a low quantitative value, the trend of more functional groups in rGO_2 is in good agreement with more accurate XPS results.
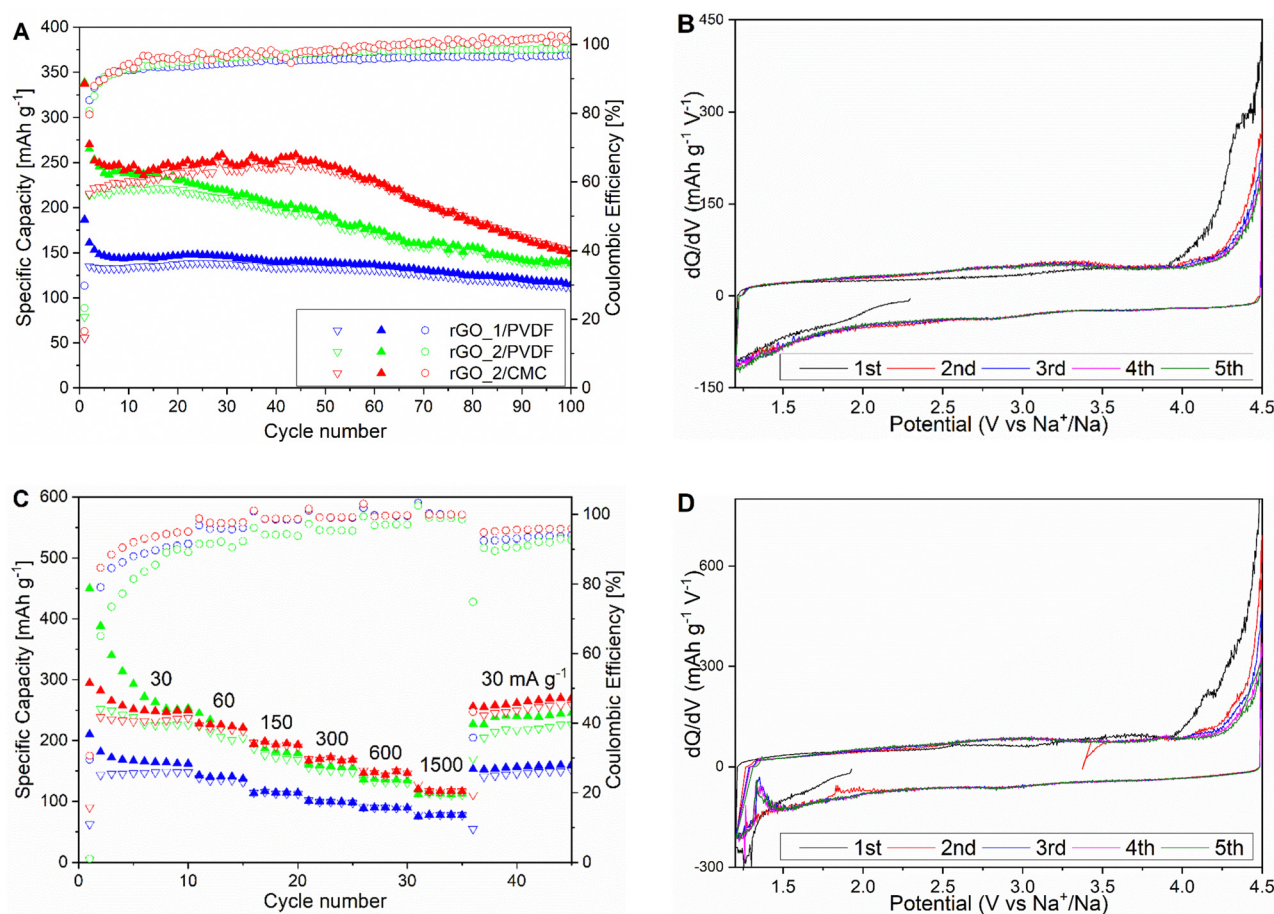
Electrochemical performance

The electrochemical performance of both reduced graphene oxide samples was evaluated in half-cells using galvanostatic cycling. The electrodes were cycled against Na metal in the 1.2–

4.5 V potential window at a current rate of 30 mA g^{-1} (Fig. 3) using 1 M NaClO_4 in EC:PC 1:1 as electrolyte. The first charge showed a remarkable capacity of 338 mA h g^{-1} and 187 mA h g^{-1} for rGO_2 and rGO_1, respectively. The initially low Coulombic efficiency is attributed to the formation of the SEI passivation layer, a common phenomenon in high surface area carbonaceous materials. After 10 cycles, both electrodes stabilized and exhibited a reversible discharge capacity of 220 mA h g^{-1} and 133 mA h g^{-1} and an average Coulombic efficiency of 97.2% and 95.4%, respectively. This difference in capacity between the two materials can be mainly attributed to differences in the specific surface area, i.e. rGO_2 has almost double the surface area and capacity compared to rGO_1. In fact, the discharge capacity and surface area of rGO_2 are close to the values reported by Ali et al.[22] However, significant continuous capacity fading was observed in the rGO_2 sample with only 47% of the capacity of the 10th cycle observed at the 100th cycle, while rGO_1 was more stable and 82% of the second cycle capacity was retained after 100 cycles. The observed small capacity fluctuations in both samples can be explained by changes in ambient temperature during cycling.

It is known that careful choice of the binder used in electrode fabrication can greatly influence the electrochemical performance upon cycling, owing to its ability to maintain structural integrity upon volume changes and negligible inter-actions with the electrolyte.[57–59] The PVDF binder is commonly used in LIB cathodes, yet for sodium chemistries, CMC is emerging as the binder of choice thanks to its low toxicity and high stability in sodium electrolytes.[60] Another rGO_2 electrode was therefore prepared with CMC instead of the PVDF binder, with the aim of maintaining its high capacity and

Fig. 3 Electrochemical performance of two rGO cathodes. (A) Galvanostatic cycling of rGO_1 and rGO_2 cathodes with PVDF binder and rGO_2 with CMC binder. The electrodes were cycled at 30 mA g^{-1} in 1.2–4.5 V voltage window. (B) and (D) The extracted dQ/dE vs. V curves of first 5 cycles of cathodes rGO_1/PVDF (B) and rGO_2/PVDF (D). (C) Rate capability of rGO_1 and rGO_2 cathodes with PVDF binder and rGO_2 with CMC binder. Legend as in (A).

extending cycle life. Cycling results (Fig. 3(A)) show that the stability of the electrode was noticeably improved. Indeed, no capacity fading was observed in the first 50 cycles retaining 241 mA h g^{-1}. Moreover, the average Coulombic efficiency was as high as 98.7% indicating enhanced reversibility. Nonetheless, the capacity started to diminish rapidly after 50 cycles, resulting in less-than-ideal overall performance, which might suggest the presence of some degradation mechanism.

Rate capabilities of both cathodes were studied at 30, 60, 150, 300, 600 and 1500 mA g^{-1} current densities (Fig. 3(C)). The rGO_2/CMC maintained the high capacity of 117 mA h g^{-1} at 1500 mA g^{-1}. On the other hand, the rGO_1 based electrode achieved 76 mA h g^{-1} at the same current rate. In all cases, the electrodes retained ∼50% of the initial capacity at the highest current rate. Notably, both rGO_2/PVDF and rGO_2/CMC achieved higher capacities at 600 mA g^{-1} (respectively, 136 and 146 mA h g^{-1}) when compared with previous work.[61] Both materials restored the initial capacity after returning to 30 mA g^{-1}, indicating good stability at a high discharge current. However, capacity fading upon prolonged cycling remains an obstacle on the road to the practical utilization of high energy

and power capabilities of the rGO cathode; thus, the energy storage mechanism has to be understood to find the root cause.

The first five charge and discharge potential profiles of both cathodes with PVDF binder exhibit smooth curves without obvious plateaus (Fig. S2, ESI†), characteristic of typical EDLC behaviour,[62] in agreement with previous results.[61] This indicates that the storage mechanism is predominantly based on non-diffusion limited surface reactions, in line with the observed good stability at high current rates. This is reflected in the higher capacity of rGO_2, which has more open and exposed graphene flakes with a higher specific surface area, facilitating better electrolyte penetration and more accessible surfaces compared to the compact rGO_1 particles.

The potential derivatives of the specific capacity curve (dQ/dV vs. V) plots give more detailed insights into the electrochemical behaviour (Fig. 3(B) and (D)). During the first charge, a significant increase in oxidation current is observed above 4.2 V, which diminishes in subsequent cycles, indicating irreversible reactions.[61] It was reported that NaClO$_4$-based electrolytes can undergo decomposition at very high potentials vs. Na/ Na$^+$ due to the oxidizing nature of ClO$_4^-$ anions.[63–65]

Additionally, nitrogen atoms lower the energy barrier and can catalyse ClO_4^- degradation.[66,67] The effect of nitrogen-induced electrolyte oxidation above 4.2 V was also observed in the mesoporous graphene cathode for Na-ions.[37] These results point toward a scenario where above 4.2 V, irreversible oxidation of the electrolyte limits the cycle life of the cell, a phenomenon that is more pronounced in the rGO_2 electrode, which has a higher nitrogen content.

In subsequent cycles, the dQ/dV curves of both rGO samples show small, broad features between 2.2 V and 3.5 V on charge and at 2.9 V on discharge, indicating reversible redox reactions. The rGO_2 cathode also displayed an unusual dQ/dV feature at 1.3 V on the discharge curve, potentially due to contamination from H_2O produced during perchlorate anion reduction.[68–70]

Notably, replacing the PVDF binder with CMC did not affect the potential curve shapes (Fig. S4, ESI†). To better understand the origin of the faradaic components, the reactions occurring upon cycling and the causes of capacity degradation, the sodium storage mechanism in rGO cathodes was further studied using *in situ* Raman spectroscopy and *in situ* X-ray PDF measurements.

Energy storage mechanism

In situ Raman spectroscopy is a very powerful tool for elucidating electrochemical storage mechanisms as well as cycling-induced degradation and SEI formation in a variety of systems. In carbonaceous materials, the technique has been pivotal for the understanding of lithium and sodium uptake thus allowing the design of optimized materials through changes in a number of defects, heteroatom doping and degree of graphitization.[35,71–73] In the case of rGO, *in situ* Raman spectroscopic measurements could provide insights into the nature of the reversible and irreversible reactions occurring throughout the entire potential window. Spectra were therefore collected during the cyclic voltammetry for both cathodes. The results of the first two de/sodiation cycles of rGO_2, narrowed to D and G band doublet, are shown in Fig. 4(A). At the open circuit potential, both D and G bands are observed at 1350 cm^{-1} and 1600 cm^{-1}, respectively. The most
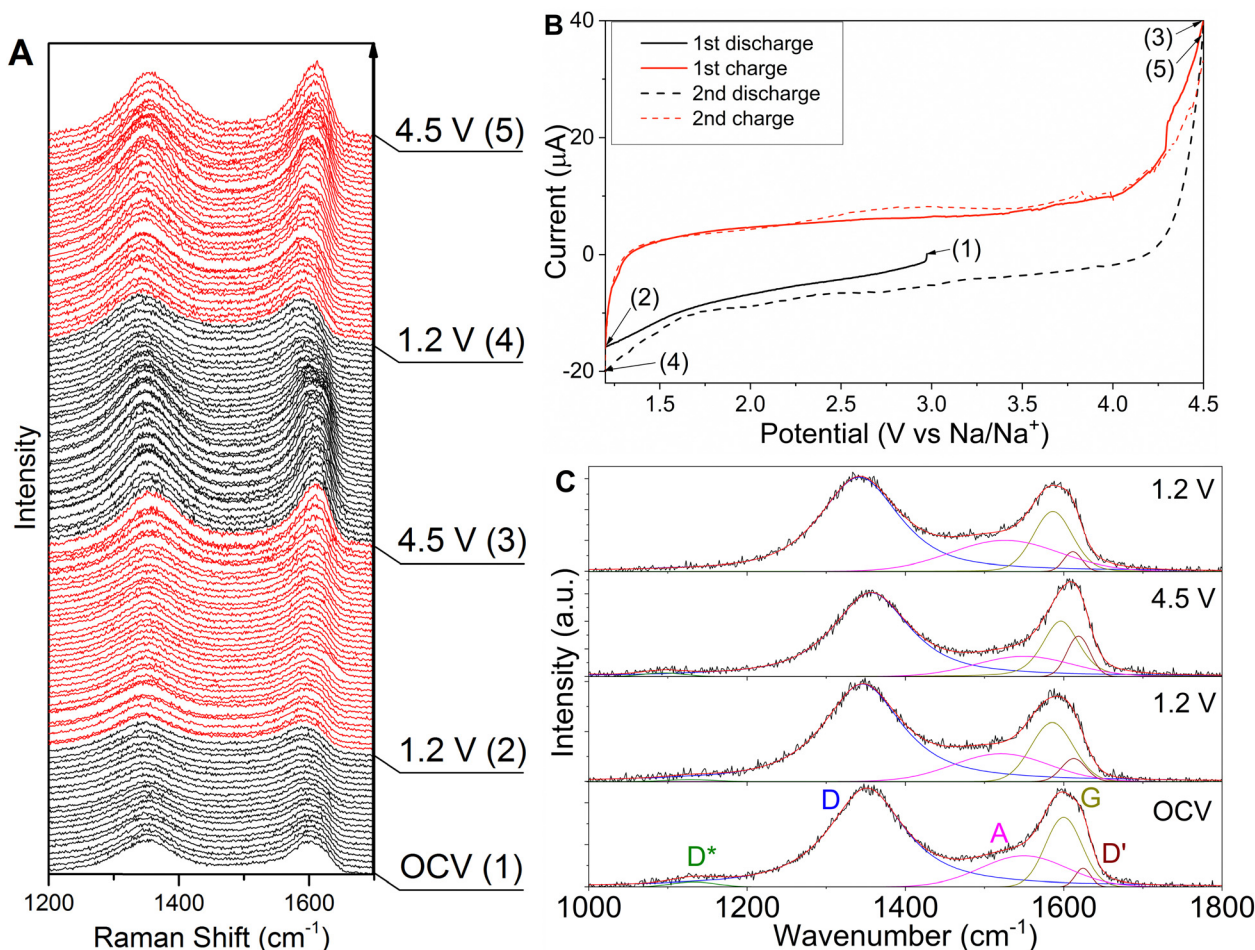
Fig. 4 *In situ* Raman measurements of rGO_2 cathode. (A) Stacked Raman spectra of rGO_2 cathode in the first two de/sodiation cycles. Arrow indicates direction of voltage changes. Each spectrum relates to approximately 0.1 V potential change. Numbers in parentheses correspond to points on CV profile (B). Black lines correspond to sodiation and red lines to desodiation. (B) Cyclic voltammetry (CV) profile from *in situ* Raman measurement of rGO_2 cathode. The scan rate is 0.2 mV s^{-1}. Black lines correspond to sodiation and red lines to desodiation. (C) Fitted Raman spectra of rGO_2 cathode at OCV and cut off potentials.

prominent change in Raman spectra during the first sodiation is the continuous red shifting of the G band to reach 1590 cm^{-1} at 1.2 V. This behaviour is in contrast to reports of lithiation mechanism in graphite, where an upshift of the G band, followed by splitting into the $E_{2g2}(i)$ and $E_{2g2}(b)$ modes were reported.[40,41,74,75] The Raman data, therefore, suggest no intercalation of Na$^+$ ions within the rGO layers. This is also confirmed by the corresponding CV plot that shows the absence of any feature which could be ascribed to intercalation and by no significant change in the position of the [002] peak in the *ex situ* XRD pattern (Fig. S3, ESI†). On the other hand, the downshift of the G band has been associated with the transition to the n-doped state of graphene.[76–80] Therefore, the gradual shift of the G band in rGO_2 can be ascribed to the change in the general electrical state caused by Na$^+$ uptake.

In the reverse scan (desodiation), a major blue shift (Δ = 12 cm^{-1}) and a sharpening of the G band (Δ = −8 cm^{-1}) are observed. This change is linear in the whole potential window. The G band returns to the position observed at OCV at around 3.5 V, which corresponds to the switch from the n-doped state back to the neutral state. Above 3.5 V, the changes continue in the same manner. The frequency shift and sharpening of the G band have been linked to the changes in the Fermi surface of graphene due to the p-doping effect.[77,81] In the functionalised rGO and organic electrodes, the reversible association and dissociation of electrolyte anions (ClO$_4^-$ or PF$_6^-$) on the material's surface above 3.0 V vs. Li/Li$^+$ (2.7 V vs. Na/Na$^+$) was reported.[20,82–84] This leads to charge transfer and the formation of the [(RN)$^{+x}$A$_x^-$] complex, for example [(N)$^{+x}$(PF$_6^-$)$_x$],[83] causing the creation of the p-doped state of reduced graphene oxide. Hence, the oxidative current increase above 3.5 V, correlated with the significant blue shift and sharpening of the G band in the Raman spectra of rGO_2, is at least partly associated with p-doping from ClO$_4^-$ anions association. However, the presence of NaCl in the electrode indicates that the part of the charge reaction above 4.2 V is related to the irreversible electrolyte decomposition.[68] The ClO$_4^-$ reduction can additionally be catalysed by the presence of nitrogen atoms.[67,85–87]

Nevertheless, in the second discharge, no G band changes down to 3.5 V were observed. This indicates that the negative charge from ClO$^-$ maintained the p-doped state of rGO. Starting from 3.5 V, a red shift of the G band was detected, which demonstrates the disassociation of ClO$^-$ anions, *i.e.* the reversal of the p-doping. Additionally, the largest change in the G band position occurs between 3.0 V and 2.5 V, which is correlated with a reduction peak at 2.9 V. Recent studies on functionalised rGO, GO or CNT electrodes for LIBs reported on reversible reduction and oxidation of oxygenic functional groups in reaction C=O + Li$^+$ + e$^-$ $\leftrightarrow$ C–O–Li.[13–17,82,88,89] Therefore, the 2.9 V reduction peak and the corresponding downshift of the G band can be attributed to the Na$^+$ redox reaction with the oxygen functional groups on the reduced graphene oxide surface: C=O + Na$^+$ + e$^-$ $\leftrightarrow$ C–O–Na.[14,20,83,88] At 1.2 V, the G band position is the same as in the first discharge, confirming the reversible formation of the n-doped state. Similarly, for the second charge, the G band blue shift is repeated, as well as the oxidation peaks at 2.7 V and

3.25 V, indicating that the redox reaction with functional groups and the p-doping of rGO are reversible.

The *in situ* Raman measurement rGO_1 sample was conducted as well, and the spectra of the first two discharge/charge cycles showed a similar pattern to rGO_2. For a detailed study and comparison, the spectra of both samples at OCV and cut-off potentials were fitted with 5 peaks as described earlier (Fig. 4(C) and Fig. S5, ESI†). Fig. 5 shows key Raman parameters plotted *versus* cell potential. It was observed that the G peak component of the G band (Fig. S6A, ESI†) shifts to a lower wavenumber on discharge. Interestingly, initially in the rGO_2 electrode, the G peak was located at a higher wavenumber due to the nitrogen content; however, at 1.2 V, it is the same (1585 cm^{-1}) for both samples. This indicates that the influence of the N lone-pair electrons on phonon dispersion is neutralised and Na–N bonds are formed, which increases rGO_2 capacity analogously to Li-ion systems.[83] When the cells were charged to 4.5 V, the G peak returned to the frequency just below the OCV position. Therefore, the apparent major blue shift of the G band described above is in fact caused by the increase in the D$'$ peak intensity (red colour in Fig. S6A, ESI†). The increase in the $I_{D'}/I_G$ ratio during the oxidation scan is ascribed to the release of Na$^+$ and consequent oxidation of epoxy functional groups[15] followed by ClO$_4^-$ anions association on the surface of rGO and p-doping. Additionally, the changes in the FWHM of the G peak (Fig. S6B, ESI†) in the rGO_2 sample confirm the p-doping – *i.e.* stiffening at 4.5 V was observed. This effect was less obvious in rGO_1 due to the lower nitrogen content and the absence of pyridinic groups.[83] In the second discharge, the $I_{D'}/I_G$ ratio and FWHM returned to previous values, indicating that this mechanism is reversible.

The defect concentration in the carbon materials is mainly associated with the D/G peaks intensity ratio (Fig. S6A, ESI†). During the CV scan of both samples, the I_D/I_G ratio is very close and changes accordingly with sodium de/insertion. It increases with discharge and decreases with charge. Additionally, a corresponding increase and decrease in the FWHM of the D peak is observed (Fig. S6B, ESI†). This suggests that sodium intake increases the defect concentration in rGO, while its release has the reverse effect. This is also reflected in the I_A/I_G ratio (Fig. S6C, ESI†) linked to the amorphous portion of the rGO, which increases at 1.2 V and drops at 4.5 V. The I_{D*}/I_G ratio (Fig. S6C, ESI†) is associated with the sp^2–sp^3 bonds at the edges of graphene layers. In the first discharge of both samples, at 1.2 V, the intensity of the D* peak is significantly reduced, while in the subsequent charge, reverse change is observed. This behaviour indicates the storage of Na$^+$ ions at the edges of graphene layers.[19] Moreover, the I_{D*}/I_G ratio at 4.5 V is close to its value at OCV, suggesting that ClO$_4^-$ anions associate rather at the basal plane of rGO, contrary to Na$^+$ storage at the edges. The decrease appeared again in the second discharge, confirming the reversibility of the process.

To gain further insights into the storage mechanism, *in situ* X-ray total scattering measurements were performed to study real-time local structural changes during cycling. As no significant difference between rGO_1 and rGO_2 was observed, only
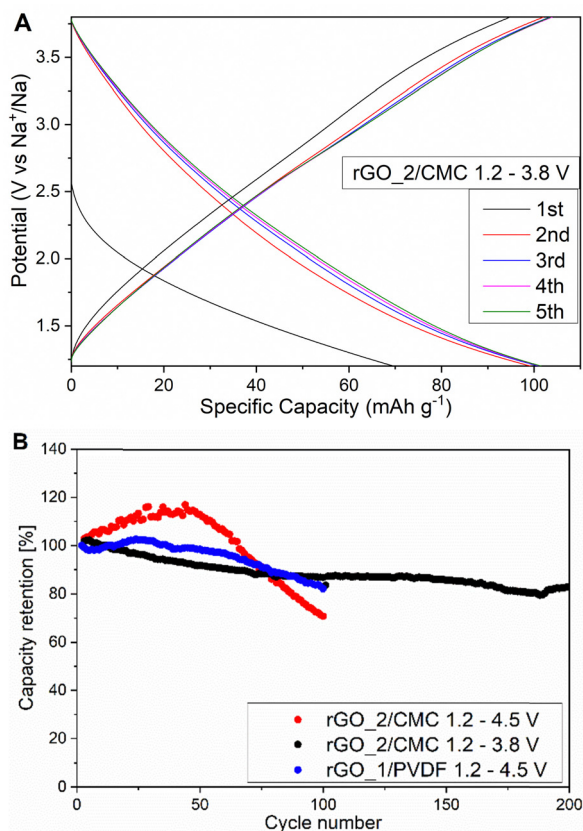
Fig. 5 De/sodiation mechanism of rGO cathode. (A) Evolution of experimental PDF curves during the electrochemical cycling. The colour of the dashed lines refers to the graphics of panel B. (B) Sketch of C atomic arrangement within a graphene layer. The circles indicate regions at the same radial distance from a C atom located in the centre.

the latter was analysed in detail. The experimental patterns (Fig. S7, ESI†) collected *in situ* at different potentials, corresponding to maximum sodiation and desodiation, reveal no signification variation. This indicates that there are no significant structure changes in the bulk of rGO during cycling. Similarly, the corresponding PDF data reported in Fig. 5(A), obtained from the Fourier transform of the corrected and normalized total scattering data, show no changes with the peak positions remaining constant within 0.01 Å.

The experimental PDF shows only three well-defined peaks, indicating the absence of long-range order, in agreement with the diffraction data. The first peak occurs at 1.4 Å, which is consistent with the tabulated C–C bond length for graphene (1.42 Å). No evidence of the C–O bond is observed because of their low frequency and the similarity with the C–C distances. The PDF intensity is generally averaged over all atom pairs, and therefore the observed signal is dominated by C–C correlations of the graphene skeleton. In order to understand the origin of the other two peaks located at 2.4 Å and 3.7 Å a graphene layer should be considered. Even though experimental PDF studies on graphene are scarce, examples of calculated PDF are given in the work of Kumar *et al.*[90] and these are obtained by considering a model where every C atom lies at the intersection of three C_6

hexagons (Fig. 5(B)). Centring on this C atom and assuming a flat layer, one can draw circles intercepting the next C atoms and each circle corresponds to an interatomic distance, *i.e.* a positive correlation in the PDF. The second peak corresponds to the 2nd and 3rd neighbours within a hexagon. As the peak at 2.8 Å has a lower multiplicity, it is hidden in the background. According to this model, the presence of a clear peak in the experimental PDF at 2.4 Å indicates a coherent region composed of 3 hexagons. The third PDF peak is broader with lower intensity and even broader features are observed at larger interatomic distances. These should correspond to the centre of mass of nearby C_6 hexagons, not arranged coherently because of the presence of defects. The results indicate that atomic structure is well ordered only within a few hexagons while the layer is disordered, or corrugated, so that rigid correlation between far hexagons is lost. As no changes are observed in the PDF data when the rGO cathodes were cycled in the full potential widow, it follows that the structural disorder induced by the sodiation/desodiation process is negligible compared to that already present in the pristine samples. Furthermore, the obtained PDF data do not show changes in peak position or width upon cycling, implying that interlayer expansion and contraction occurring during discharge and charge can be ruled out. This infers the absence of an intercalating behaviour and the lack of charge transfer between sodium and the p-band of the graphene sheet.

The detailed analysis presented describes a scenario where the storage mechanism of rGO as a cathode is pseudocapacitive-like, predominantly based on the absorption of ions on the surface of the graphene-like sheets. The more open and exposed morphology of rGO_2 flakes compared to the closed and compact particles of rGO_1 supports more extensive electrolyte penetration and more sites for ion storage, resulting in a higher specific capacity.[91] However, other reactions also take place, playing a major role in determining the electrochemical performance, contributing to the total capacity as well as defining the long-term cycling stability. Particularly, the faradaic mechanism can be divided into two stages. First, below 3.5 V, the Na+ ions are stored at the defects and edges of rGO and through redox reaction with the O and N functional groups. Then, above 3.5 V, the association of anions from the electrolyte on the rGO basal plane occurs. These processes are seen in the *in situ* Raman as a continuous and linear transition from the p-doped state (oxidised state) to the n-doped state (reduced state). However, these are not observable in the PDF data as they apply to a fraction of the material and do not induce structural changes in the bulk. In the rGO_2 electrode, the nitrogen content improves the specific capacity, owing to coordination interaction between Na and N lone-pair electrons (Na–N bonding)[83] as well as increased absorption of ClO_4^- anions near N-functional groups.[67,85] However, the heteroatoms also act as catalysts for electrolyte degradation above 4.2 V, causing capacity fade. The capacity loss is smaller in the rGO_1 due to lower nitrogen content, but the effect on cycle life is still rather significant.

It is worth noting that a similar mechanism of utilisation electrolyte salt anions as charge carriers has been applied in so-called 'dual ion' batteries.[92] However, in this case, the anions

are stored in a graphite cathode *via* an intercalation mechanism, which delivers relatively low capacities. For instance, Fan *et al.* reported on soft carbon-graphite Na-ion 'dual carbon' cell, where graphite cathode delivered a small capacity of around 40 mA h g^{-1},[93] or in another example, the graphitic cathode presented a capacity of $\sim$60 mA h g^{-1} in a full cell with the hard carbon anode.[94] In the case of the rGO cathode, the anions are stored on the surface of graphene sheets, which provides higher capacity and better kinetics.

Improving cycle life and proof-of-concept full cell

To avoid harmful reactions above 4.2 V and improve the electrode cycle life, the upper cut-off potential was decreased to 3.8 V. The potential profiles of rGO_2 cycled between 1.2–3.8 V are shown in Fig. 6(A). The first charge capacity was 95 mA h g^{-1},
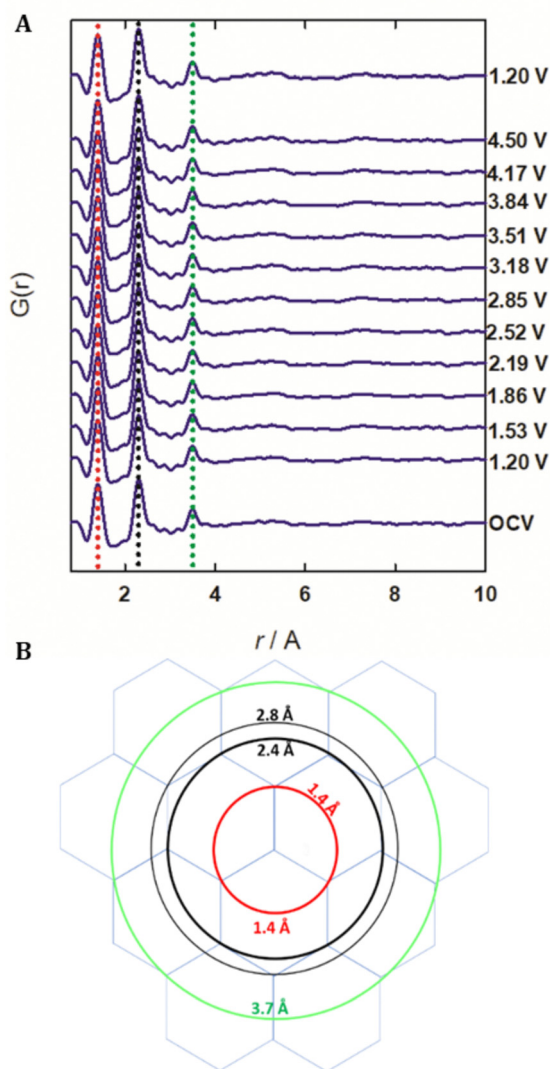
Fig. 6 Improved cycle life of rGO cathode. (A) Voltage profiles of first 5 cycles of rGO_2 with CMC binder cycled in narrowed 1.2–3.8 V voltage window. (B) Capacity retention comparison between electrodes cycled in 1.2–4.5 V voltage window (red and blue) and narrowed 1.2–3.8 V window (black). Percentage value was calculated in relation to second discharge.
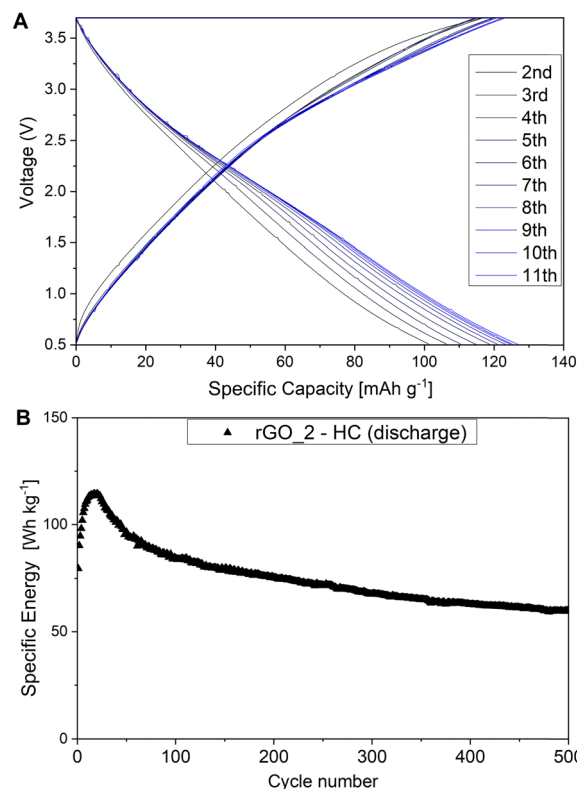
Fig. 7 Electrochemical performance of all carbon full cell. (A) Voltage profiles of first of rGO_2/CMC − HC full cell cycled in 0.5–3.7 V voltage window. (B) Energy density performance of full cell during long galvanostatic cycling.

which is lower compared to the full potential window cell, partly due to omitting the majority of the second stage of the storage mechanism, *i.e.* ClO$_4^-$ anions association, but mostly due to avoiding electrolyte oxidation. In fact, the first cycle coulombic efficiency was as high as 73.5% and averaged at 99.2% in the following cycles, indicating that the electrolyte decomposition was significantly averted demonstrating that rGO is a robust cathode material. The rGO cathode showed very good stability over 200 cycles. The capacity retention of rGO_2 cycled in both potential windows and rGO_1 is compared as shown in Fig. 6(B).

To demonstrate the feasibility of a reduced graphene oxide cathode, rGO_2 was coupled with a hard carbon anode and a full cell galvanostatic cycling was carried out. The performance of hard carbon anode is presented in Fig. S8 (ESI†). The full cell cycling was performed with a current density of 30 mA g^{-1} in a narrowed potential window (0.5–3.7 V) to avoid electrolyte decomposition. The upper and lower cut-off voltages were derived from stable half-cell measurements (3.8–1.2 V) and then adjusted to 3.7 V and 0.5 V, respectively, to accommodate the anode's working potential window (0.1–1 V). Only the rGO cathode was presodiated prior to assembly. Fig. 7(A) shows the charge–discharge profiles of cycles 2–11th of the full cell. The charge–discharge curves reflected the sloping shape observed in the half cell. The discharge capacity achieved after the formation cycle was 101 mA h g^{-1} (based on the cathode active mass). In the first 10 cycles, the capacity was increased to

reach 125 mA h g^{-1}. A similar increase was observed for the rGO_2 half cells and can be ascribed to the opening of the rGO structure and the gradual electrolyte penetration into the electrode.[22] An additional effect has the balancing of anode and cathode potentials, as the capacity ratio was not perfectly matched. Based on the total mass of the cathode and anode active materials and average discharge potential of 1.85 V, the specific energy of the full cell is calculated to be 80 W h kg^{-1}. For comparison, similar energy density was achieved with the rGO/Sb$_2$S$_4$–Na$_2$/3Ni$_{1/3}$Mn$_{2/3}$O$_2$ system, which consists of much more expensive and less sustainable transition metals.[95] Moreover, the rGO_2 – HC full cell showed remarkable stability over 500 cycles, which is reflected in a capacity loss of only 0.05% per cycle. Further optimisation of electrode materials, potential windows and electrolytes can significantly improve the energy density.

Conclusions

Two reduced graphene oxides varying in morphology and chemical structure were presented as promising cathode materials for SIBs. The rGO_1 material has a particle-like morphology and consists of a larger number of hydroxyl/epoxy functional groups, while rGO_2 has an open structure comprising thin creased sheets sized 0.1–1 μm and has a higher content of oxygen and nitrogen functional groups. The rGO_1 and rGO_2 cathodes showed high reversible capacities of 133 mA h g^{-1} and 220 mA h g^{-1}, respectively, in a potential window of 1.2–4.5 V. Higher capacity of the latter is ascribed to a more accessible morphology and higher content of functional groups, particularly nitrogenic. Nonetheless, cycle life was not satisfactory, even when enhanced by replacing PVDF with CMC binders.

Detailed *in situ* Raman spectroscopy and PDF measurements shed light on the electrochemical processes. Both techniques ruled out ion intercalation commonly observed in graphite electrodes. Instead, the energy storage mechanism relied on surface reactions and was divided into two stages, one depending on the Na$^+$ ions intake below 3.5 V, and a second process above 3.5 V, which involved the association of anions from the electrolyte on the rGO surface. It was found that Na$^+$ ions are stored mainly on the defects and edges of rGO as well as *via* redox reaction with the functional groups: C=O + Na$^+$ + e$^-$ ↔ C–ONa. Moreover, functional groups containing nitrogen increased the capacity by offering more reaction sites for Na$^+$ ions. At the higher potentials, the perchlorate anions from the NaClO$_4$ salt associate on the graphene basal plane. The N-heteroatoms enhanced the adsorption of ClO$_4^-$ anions, however also amplified decomposition to NaCl causing severe electrolyte degradation. All these mechanisms are predominantly surface reactions, which ensure good rate capability and high structural stability of electrodes. This also indicates that optimisation of both materials morphology and chemical structure can result in excellent performance.

To avoid severe electrolyte decomposition above 4.2 V, a narrower cut-off potential was applied. Although this resulted in decreased capacity, as the p-doping region was not fully utilized, the cycle life was greatly improved. Therefore, careful selection of more stable electrolytes can make high capacity and long cycle life rGO cathodes possible.

As a proof-of-concept, a full cell with rGO_2/CMC cathode and hard carbon anode was assembled. It showed a specific energy of 80 W h kg^{-1} and outstanding stability over 500 cycles, proving that rGO is a viable SIBs' cathode material candidate. Replacing transition metal oxides with carbonaceous cathodes could solve environmental and economic concerns and lead to a significant reduction in the overall manufacturing costs of SIBs. The gained comprehensive understanding of the energy storage mechanism in rGO electrodes can be applied to design high-performance carbonaceous cathodes for SIBs. This can render the commercialisation of all-carbon SIBs viable as a low-cost and sustainable solution for different applications, particularly for medium- to large-scale energy storage.

Data availability

Data for this article is available at Zenodo at **https://doi.org/10.5281/zenodo.11472557**.

Conflicts of interest

There are no conflicts to declare.

Acknowledgements

References

1 Y. Kim, K. H. Ha, S. M. Oh and K. T. Lee, *Chem. – Eur. J.*, 2014, **20**, 11980–11992.

2 J. Kim, H. Kim and K. Kang, *Adv. Energy Mater.*, 2018, **8**, 1702646.

3 J. Speirs, M. Contestabile, Y. Houari and R. Gross, *Renewable Sustainable Energy Rev.*, 2014, **35**, 183–193.

4 C. Vaalma, D. Buchholz, M. Weil and S. Passerini, *Nat. Rev. Mater.*, 2018, **3**, 18013.

5 J.-Y. Hwang, S.-T. Myung and Y.-K. Sun, *Chem. Soc. Rev.*, 2017, **46**, 3529–3614.

6 D. Saurel, B. Orayech, B. Xiao, D. Carriazo, X. Li and T. Rojo, *Adv. Energy Mater.*, 2018, **8**, 1703268.

7 B. Zhang, C. M. Ghimbeu, C. Laberty, C. Vix-Guterl and J. M. Tarascon, *Adv. Energy Mater.*, 2016, **6**, 1–9.

8 K. Gotoh and H. Ishida, *Carbon*, 2014, **78**, 633.

9 S. Komaba, W. Murata, T. Ishikawa, N. Yabuuchi, T. Ozeki, T. Nakayama, A. Ogata, K. Gotoh and K. Fujiwara, *Adv. Funct. Mater.*, 2011, **21**, 3859–3867.

10 W. J. Li, C. Han, W. Wang, F. Gebert, S. L. Chou, H. K. Liu, X. Zhang and S. X. Dou, *Adv. Energy Mater.*, 2017, **1700274**, 1–10.

11 Y. Li, Y. Lu, C. Zhao, Y.-S. Hu, M.-M. Titirici, H. Li, X. Huang and L. Chen, *Energy Storage Mater.*, 2017, **7**, 130–151.

12 M.-S. Balogun, Y. Luo, W. Qiu, P. Liu and Y. Tong, *Carbon*, 2016, **98**, 162–178.

13 X. Han, C. Chang, L. Yuan, T. Sun and J. Sun, *Adv. Mater.*, 2007, **19**, 1616–1621.

14 S. W. Lee, N. Yabuuchi, B. M. Gallant, S. Chen, B.-S. Kim, P. T. Hammond and Y. Shao-Horn, *Nat. Nanotechnol.*, 2010, **5**, 531–537.

15 H. R. Byon, B. M. Gallant, S. W. Lee and Y. Shao-Horn, *Adv. Funct. Mater.*, 2013, **23**, 1037–1045.

16 H. Kim, H.-D. Lim, S.-W. Kim, J. Hong, D.-H. Seo, D. Kim, S. Jeon, S. Park and K. Kang, *Sci. Rep.*, 2013, **3**, 1506.

17 H. Kim, K.-Y. Park, J. Hong and K. Kang, *Sci. Rep.*, 2015, **4**, 5278.

18 D. Xiong, X. Li, H. Shan, Y. Zhao, L. Dong, H. Xu, X. Zhang, D. Li and X. Sun, *Electrochim. Acta*, 2015, **174**, 762–769.

19 D. Xiong, X. Li, H. Shan, B. Yan, D. Li, C. Langford and X. Sun, *Appl. Energy*, 2016, **175**, 512–521.

20 D. Xiong, X. Li, Z. Bai, H. Shan, L. Fan, C. Wu, D. Li and S. Lu, *ACS Appl. Mater. Interfaces*, 2017, **9**, 10643–10651.

21 B. Wang, T. Ruan, Y. Chen, F. Jin, L. Peng, Y. Zhou, D. Wang and S. Dou, *Energy Storage Mater.*, 2020, **24**, 22–51.

22 G. Ali, A. Mehmood, H. Y. Ha, J. Kim and K. Y. Chung, *Sci. Rep.*, 2017, **7**, 40910.

23 A. Goñi, A. Iturrondobeitia, I. Gil de Muro, L. Lezama and T. Rojo, *J. Power Sources*, 2017, **369**, 95–102.

24 A. Li, Z. Feng, Y. Sun, L. Shang and L. Xu, *J. Power Sources*, 2017, **343**, 424–430.

25 F. Mazzali, M. W. Orzech, A. Adomkevicius, A. Pisanu, L. Malavasi, D. Deganello and S. Margadonna, *ACS Appl. Energy Mater.*, 2019, **2**, 344–353.

26 R. Thangavel, A. G. Kannan, R. Ponraj, X. Sun, D.-W. Kim and Y.-S. Lee, *J. Mater. Chem. A*, 2018, **6**, 9846–9853.

27 H. Kim, K.-Y. Park, J. Hong and K. Kang, *Sci. Rep.*, 2015, **4**, 5278.

28 H. Kim, H.-D. Lim, S.-W. Kim, J. Hong, D.-H. Seo, D. Kim, S. Jeon, S. Park and K. Kang, *Sci. Rep.*, 2013, **3**, 1506.

29 S. W. Lee, N. Yabuuchi, B. M. Gallant, S. Chen, B.-S. Kim, P. T. Hammond and Y. Shao-Horn, *Nat. Nanotechnol.*, 2010, **5**, 531–537.

30 X. Han, C. Chang, L. Yuan, T. Sun and J. Sun, *Adv. Mater.*, 2007, **19**, 1616–1621.

31 H. R. Byon, B. M. Gallant, S. W. Lee and Y. Shao-Horn, *Adv. Funct. Mater.*, 2013, **23**, 1037–1045.

32 J. Zou, C. Sole, N. E. Drewett, M. Velický and L. J. Hardwick, *J. Phys. Chem. Lett.*, 2016, **7**, 4291–4296.

33 C. Sole, N. E. Drewett and L. J. Hardwick, *Faraday Discuss.*, 2014, **172**, 223–237.

34 W. Huang, *J. Electrochem. Soc.*, 1998, **145**, 765.

35 S. Migge, G. Sandmann, D. Rahner, H. Dietz and W. Plieth, *J. Solid State Electrochem.*, 2005, **9**, 132–137.

36 S. Bose, T. Kuila, A. K. Mishra, R. Rajasekar, N. H. Kim and J. H. Lee, *J. Mater. Chem.*, 2012, **22**, 767–784.

37 X. Zhu, Q. Jiang, T. Wang, Q. Zhang, X. Jia and R. Zhang, *ChemSusChem*, 2019, **12**, 4323–4331.

38 J. Zhang, W. Lv, Y. Tao, Y. B. He, D. W. Wang, C. H. You, B. Li, F. Kang and Q. H. Yang, *Energy Storage Mater.*, 2015, **1**, 112–118.

39 H. Ma, H. Geng, B. Yao, M. Wu, C. Li, M. Zhang, F. Chi and L. Qu, *ACS Nano*, 2019, **13**, 9161–9170.

40 C. Sole, N. E. Drewett and L. J. Hardwick, *Faraday Discuss.*, 2014, **172**, 223–237.

41 J. Zou, C. Sole, N. E. Drewett, M. Velický and L. J. Hardwick, *J. Phys. Chem. Lett.*, 2016, **7**, 4291–4296.

42 P. Juhás, T. Davis, C. L. Farrow and S. J. L. Billinge, *J. Appl. Crystallogr.*, 2013, **46**, 560–566.

43 A. J. Stapleton, C. J. Shearer, C. T. Gibson, A. D. Slattery and J. G. Shapter, *Nanotechnology*, 2016, **27**, 125704.

44 D. Xiong, X. Li, Z. Bai, H. Shan, L. Fan, C. Wu, D. Li and S. Lu, *ACS Appl. Mater. Interfaces*, 2017, **9**, 10643–10651.

45 W. J. Lee, J. Lim and S. O. Kim, *Small Methods*, 2017, **1**(1–2), 1600014.

46 G. Freihofer, S. Raghavan and D. Gosztola, *Appl. Spectrosc.*, 2013, **67**, 321–328.

47 S. Claramunt, A. Varea, D. López-Díaz, M. M. Velázquez, A. Cornet and A. Cirera, *J. Phys. Chem. C*, 2015, **119**, 10123–10129.

48 Y. Wang, D. C. Alsmeyer and R. L. McCreery, *Chem. Mater.*, 1990, **2**, 557–563.

49 A. Sadezky, H. Muckenhuber, H. Grothe, R. Niessner and U. Pöschl, *Carbon*, 2005, **43**, 1731–1742.

50 S. Osswald, M. Havel and Y. Gogotsi, *J. Raman Spectrosc.*, 2007, **38**, 728–736.

51 G. X. Chen and H. Shimizu, *Polymer*, 2008, **49**, 943–951.

52 P. Venezuela, M. Lazzeri and F. Mauri, *Phys. Rev. B: Condens. Matter Mater. Phys.*, 2011, **84**, 035433.

53 A. Cuesta, P. Dhamelincourt, J. Laureyns, A. Martínez-Alonso and J. M. D. Tascón, *J. Mater. Chem.*, 1998, **8**, 2875–2879.

54 A. C. Ferrari and J. Robertson, *Phys. Rev. B: Condens. Matter Mater. Phys.*, 2000, **61**, 14095–14107.

55 B. Gupta, N. Kumar, K. Panda, V. Kanan, S. Joshi and I. Visoly-Fisher, *Sci. Rep.*, 2017, **7**, 1–14.

56 W. Ai, Z. Du, Z. Fan, J. Jiang, Y. Wang, H. Zhang, L. Xie, W. Huang and T. Yu, *Carbon*, 2014, **76**, 148–154.

57 L. El Ouatani, R. Dedryvère, J.-B. B. Ledeuil, C. Siret, P. Biensan, J. Desbrières and D. Gonbeau, *J. Power Sources*, 2009, **189**, 72–80.

58 J. Huesker, L. Froböse, A. Kwade, M. Winter and T. Placke, *Electrochim. Acta*, 2017, **257**, 423–435.

59 L. O. Vogt, M. El Kazzi, E. Jämstorp Berg, S. Pérez Villar, P. Novák and C. Villevieille, *Chem. Mater.*, 2015, **27**, 1210–1216.

60 K. Kubota and S. Komaba, *J. Electrochem. Soc.*, 2015, **162**, A2538–A2550.

61 G. Ali, A. Mehmood, H. Y. Ha, J. Kim and K. Y. Chung, *Sci. Rep.*, 2017, **7**, 40910.

62 S. Bose, T. Kuila, A. K. Mishra, R. Rajasekar, N. H. Kim and J. H. Lee, *J. Mater. Chem.*, 2012, **22**, 767–784.

63 S. Aladinli, F. Bordet, K. Ahlbrecht, J. Tübke and M. Holzapfel, *Electrochim. Acta*, 2017, **231**, 468–478.

64 A. Bhide, J. Hofmann, A. Katharina Dürr, J. Janek and P. Adelhelm, *Phys. Chem. Chem. Phys.*, 2014, **16**, 1987–1998.

65 A. Ponrouch, E. Marchante, M. Courty, J.-M. Tarascon and M. R. Palacín, *Energy Environ. Sci.*, 2012, **5**, 8572.

66 Y. N. Kim, Y. C. Lee and M. Choi, *Carbon*, 2013, **65**, 315–323.

67 T. M. Byrne, X. Gu, P. Hou, F. S. Cannon, N. R. Brown and C. Nieto-Delgado, *Carbon*, 2014, **73**, 1–12.

68 P. Arora, *J. Electrochem. Soc.*, 1998, **145**, 3647.

69 E. T. Urbansky, *Biorem. J.*, 1998, **2**, 81–95.

70 D. Aurbach, Y. Talyosef, B. Markovsky, E. Markevich, E. Zinigrad, L. Asraf, J. S. Gnanaraj and H. J. Kim, *Electrochim. Acta*, 2004, **50**, 247–254.

71 A. Sadezky, H. Muckenhuber, H. Grothe, R. Niessner and U. Pöschl, *Carbon*, 2005, **43**, 1731–1742.

72 Z. Wang, X. Huang, R. Xue and L. Chen, *Carbon*, 1999, **37**, 685–692.

73 M. Endo, C. Kim, T. Karaki, T. Fujino, M. J. Matthews, S. D. M. Brown and M. S. Dresslhaus, *Synth. Met.*, 1998, **98**, 17–24.

74 W. Huang, *J. Electrochem. Soc.*, 1998, **145**, 765.

75 S. Migge, G. Sandmann, D. Rahner, H. Dietz and W. Plieth, *J. Solid State Electrochem.*, 2005, **9**, 132–137.

76 A. Viinikanoja, J. Kauppila, P. Damlin, M. Suominen and C. Kvarnström, *Phys. Chem. Chem. Phys.*, 2015, **17**, 12115–12123.

77 A. Das, S. Pisana, B. Chakraborty, S. Piscanec, S. K. Saha, U. V. Waghmare, K. S. Novoselov, H. R. Krishnamurthy, A. K. Geim, A. C. Ferrari and A. K. Sood, *Nat. Nanotechnol.*, 2008, **3**, 210–215.

78 M. Bouša, O. Frank, I. Jirka and L. Kavan, *Phys. Status Solidi B*, 2013, **250**, 2662–2667.

79 M. Endo, C. Kim, T. Karaki, T. Fujino, M. J. Matthews, S. D. M. Brown and M. S. Dresslhaus, *Synth. Met.*, 1998, **98**, 17–24.

80 Z. Wang, X. Huang, R. Xue and L. Chen, *Carbon*, 1999, **37**, 685–692.

81 S. Pisana, M. Lazzeri, C. Casiraghi, K. S. Novoselov, A. K. Geim, A. C. Ferrari and F. Mauri, *Nat. Mater.*, 2007, **6**, 198–201.

82 Y. Su, Y. Liu, P. Liu, D. Wu, X. Zhuang, Z. Fan and X. Feng, *Angew. Chem., Int. Ed.*, 2015, **54**, 1812–1816.

83 Y. Huang, D. Wu, A. Dianat, M. Bobeth, T. Huang, Y. Mai, F. Zhang, G. Cuniberti and X. Feng, *J. Mater. Chem. A*, 2017, **5**, 1588–1594.

84 K. Sakaushi, E. Hosono, G. Nickerl, T. Gemming, H. Zhou, S. Kaskel and J. Eckert, *Nat. Commun.*, 2013, **4**, 1485.

85 F. Yao, Y. Zhong, Q. Yang, D. Wang, F. Chen, J. Zhao, T. Xie, C. Jiang, H. An, G. Zeng and X. Li, *J. Hazard. Mater.*, 2017, **323**, 602–610.

86 Y. Shao, S. Zhang, M. H. Engelhard, G. Li, G. Shao, Y. Wang, J. Liu, I. A. Aksay and Y. Lin, *J. Mater. Chem.*, 2010, **20**, 7491–7496.

87 K. Parvez, S. Yang, Y. Hernandez, A. Winter, A. Turchanin, X. Feng and K. Müllen, *ACS Nano*, 2012, **6**, 9541–9550.

88 C. Yan, Z. Zhang, Z. Liu, Y. Liu and S. Wu, *Ionics*, 2017, **23**, 3023–3029.

89 K. Sakaushi, G. Nickerl, F. M. Wisser, D. Nishio-Hamane, E. Hosono, H. Zhou, S. Kaskel and J. Eckert, *Angew. Chem., Int. Ed.*, 2012, **51**, 7850–7854.

90 A. Kumar, M. Wilson and M. F. Thorpe, *J. Phys.: Condens. Matter*, 2012, **24**, 485003.

91 J. Smajic, A. Alazmi, N. Batra, T. Palanisamy, D. H. Anjum and P. M. F. J. Costa, *Small*, 2018, **14**(51), 1803584.

92 T. Placke, A. Heckmann, R. Schmuch, P. Meister, K. Beltrop and M. Winter, *Joule*, 2018, 1–23.

93 L. Fan, Q. Liu, S. Chen, Z. Xu and B. Lu, *Adv. Energy Mater.*, 2017, **7**, 1602778.

94 Z. Hu, Q. Liu, K. Zhang, L. Zhou, L. Li, M. Chen, Z. Tao, Y. M. Kang, L. Mai, S. L. Chou, J. Chen and S. X. Dou, *ACS Appl. Mater. Interfaces*, 2018, **10**, 35978–35983.

95 D. Y. W. Yu, P. V. Prikhodchenko, C. W. Mason, S. K. Batabyal, J. Gun, S. Sladkevich, A. G. Medvedev and O. Lev, *Nat. Commun.*, 2013, **4**, 2922.